Electrowetting-Mediated Transport to Produce Electrochemical Transistor Action in Nanopore Electrode Arrays

*Seung-Ryong Kwon, Seol Baek, Kaiyu Fu, and Paul W. Bohn**

Dr. S.-R. Kwon, Prof. P. W. Bohn
Department of Chemical and Biomolecular Engineering
University of Notre Dame, Notre Dame, IN 46556, US
E-mail: pbohn@nd.edu

S. Baek, Prof. P. W. Bohn
Department of Chemistry and Biochemistry
University of Notre Dame, Notre Dame, IN 46556, US

Dr. K. Fu
Department of Radiology and Department of Electrical Engineering
Stanford University, Stanford, CA, 94306, US

Keywords: Electrochemical transistors, electrowetting, gating, nanochannels, nanopores

Understanding water behavior in confined volumes is important in applications ranging from water purification to healthcare devices. Especially relevant are wetting and dewetting phenomena which can be switched by external stimuli, such as light and electric fields. Here, these behaviors are exploited for electrochemical processing by voltage-directed ion transport in nanochannels contained within nanopore arrays in which each nanopore presents three electrodes. The top and middle electrodes (TE and ME) are in direct contact with the nanopore volume, but the bottom electrode (BE) is buried beneath a 70 nm silicon nitride (SiN_x) insulating layer. Electrochemical transistor operation is realized when small, defect-mediated channels are opened in the SiN_x. These defect channels exhibit voltage-driven wetting that mediates the mass transport of redox species to/from the BE. When BE is held at a potential maintaining the defect channels in the wetted state, setting the potential of ME at either positive or negative overpotential results in strong electrochemical rectification

with rectification factors up to 440. By directing the voltage-induced electrowetting of defect channels, these 3-electrode nanopore structures can achieve precise gating and ion/molecule separation, and, as such, may be useful for applications such as water purification and drug delivery.

1. Introduction

Since the discovery of ion and water channels in cell membranes, great effort has been exerted to fabricate artificial biomimetic nanochannels owing to the insights they might yield into ion/water transport in confined channels as well as their promise for practical applications, such as controlled drug delivery, water purification, iontronics, and single molecular sensing.[1-10] To attain a high ion/molecule specificity, most biological channels utilize size (d ~ a few nanometers) and shape to drive effective uptake and transport of cognate ions or molecules, while rejecting unwanted species.[3, 11] The chemical functionalities along the transport pathway also play a key role in maintaining high selectivity and fast transport. For example, biological channels such as nicotinic acetylcholine receptor, potassium, and magnesium channels contain hydrophobic domains which mediate reversible wetting/dewetting processes in order to control ion/molecule transport in response to external stimuli, such as concentration gradients and electric fields.[12-15] Thus, manufacturing nanochannels with diameters < 100 nm and spatially-defined chemical functionalities along the pathway is an essential goal in order to realize smart biomimetic nanochannels.

Previous work has targeted wetting and dewetting in confined nanochannels driven by external stimuli. For example, Smirnov and coworkers demonstrated pressure-induced and voltage-driven gating response in hydrophobic nanochannels with 3 orders of magnitude difference in conductance between wetted and dewetted states,[16, 17] and Siwy and coworkers realized reversible electric-field-induced wetting and dewetting behaviors from single hydrophobic nanopores (d ~15 nm).[18] More recently, Jiang and coworkers demonstrated

dual-stimulus (light and electric field)-responsive water gating of sub-10 nm channels.[19] To date, studies have focused on characterizing and controlling external stimuli-induced wetting and dewetting of nanochannels for ion/water transport regulation, but iontronic devices, such as iontronic diodes and transistors, based on electric-field-controlled ion transport in nanochannels have not been described.

Meanwhile, our laboratory has developed several strategies for electrochemical signal amplification using dual-embedded nanopore electrode arrays (2E-NEAs). Similar to thin-layer electrochemical cells, a nanogap of ~100 nm, exists between nanopore-embedded ring or disk electrodes, thereby enabling rapid, repetitive oxidation and reduction of redox species, *i.e.*, redox cycling, resulting in highly amplified current output.[20-24] In addition, in the absence of supporting electrolyte (SE) ion accumulation and migration effects accentuate the redox cycling phenomenon, yielding up to 2000-fold total amplification.[25] Adding a charge-selective membrane, such as cation-selective Nafion, on 2E-NEAs, results in electrochemical diode behavior.[26] In addition, encapsulating attoliter-volume NEAs with a PDMS membrane produces strong current rectification and up to 250-fold signal amplification, both of which are attributed to enhanced mass transport by meniscus evolution.[27]

The versatile range of electrochemical and transport phenomena unearthed in dual-electrode NEAs suggests that even greater utility could be achieved by integrating a third electrode. Thus, we describe the fabrication and characterization of triple-embedded NEAs (3E-NEAs), in which three gold electrodes, 2 rings plus 1 disk, are embedded in each nanopore, **Figure 1**. In the 3E-NEA configuration, the top and middle ring electrodes, TE and ME, are contained within the main nanopore structure, while the bottom electrode, BE, is buried beneath a 70 nm silicon nitride (SiN_x) insulating layer. When the SiN_x layer is intact, a modest field-effect is obtained, but radical changes in redox cycling behavior are obtained when the SiN_x layer is processed under conditions that support the formation of small defect channels spanning the 70 nm SiN_x layer. In the presence of defect channels across the SiN_x, we observe redox

cycling-based current amplification using BE as a gate to govern ion transport. Furthermore, these defect channels support strong electrowetting and dewetting behavior. For example, when the BE is held at a potential maintaining the defect channels in the wetted state, setting the potential of ME at either positive or negative overpotential results in strong electrochemical rectification. The demonstration of electrowetting-mediated ion transport modulation for transistor action described here opens a new avenue to designing iontronic devices, controlled drug-release systems, and new ion/molecular separation technologies.

2. Results and Discussion

2.1. Functional Overview of 3E-NEA Fabrication and Function

To fabricate the 3E-NEA, we followed previously developed methods from this laboratory based on a combination of nanosphere lithography (NSL) and reactive-ion etching (RIE).[26-28] Briefly, ~70 nm each of gold, silicon nitride (SiN_x), gold, SiN_x, gold, and lastly 200 nm of silicon dioxide (SiO_2) were serially deposited on a glass substrate by e-beam evaporation for Au and plasma-enhanced chemical vapor deposition for SiN_x and SiO_2. It should be noted that *ca*. ±10 nm variation in the deposition thickness for nominal 70 nm SiN_x dielectric layers was observed with SEM imaging for the different batch of device fabrication. However, this variation did not produce noticeable differences in electrochemical transistor behavior. Eight independent and individually addressable NEAs (~5.5×10^4 pores in 100×100 μm^2 per array) were produced on a single glass substrate using NSL followed by RIE on lithographically-defined overlapping electrodes, Figure 1(a). RIE time was optimized so that the top and middle ring electrodes were exposed, whereas BE remained covered by a 70 nm thick SiN_x layer, Figure 1(b).

When a voltage $V > 2$ V was applied to the BE working electrode relative to the TE counter/reference electrode, dramatic changes in the nanopore electrochemical behavior were

observed, which were attributed to small pinhole-like defect channels produced through the SiN_x. These changes in the electrochemical behavior were interpreted as resulting from strong electrowetting and dewetting behaviors, as shown schematically in Figures 1(c)-(e). Furthermore, we hypothesized that robust transistor function would be observed, if the defect channels, Figure 1(c) *right*, remained in the wetted state. Depending on the potential difference between ME and BE relative to the formal potential of the test redox couple, $Fe(CN)_6^{3/4-}$, either highly amplified or inhibited redox cycling current would then be observed from ME, producing strong electrochemical rectification. These observations extend well beyond the simple diode-like functions observed in 2E-NEAs,[27] because transistor operations are driven by current pathway switching between ME-TE and ME-BE based upon electric-field-induced wetting and dewetting transitions within the SiN_x defect channels.

2.2. Redox Cycling in 3E-NEAs

Freshly prepared nanopore arrays were characterized by performing cyclic voltammetry with 100 mM $Fe(CN)_6^{3/4-}$ in 1 M KNO_3. Each of the gold layers was studied one-at-a-time by using it as a working electrode with external (*i.e.* outside the nanopore) Pt counter and Ag/AgCl reference electrodes in a 3-electrode system, while leaving the other two Au electrodes at open-circuit potential (OCP). As expected and shown in **Figure 2**(a), ME and TE showed comparable faradic responses in the absence of redox cycling, *i.e.* non-generator collector, or non-GC, mode. In addition, under these conditions only capacitive current was collected from BE due to the complete blockage of faradaic electron-transfer at BE by the SiN_x insulating layer, Figures 2(a) and S1. Next, the efficiency of redox cycling was examined by using ME and TE as generator-collector (GC) electrodes in a 4-electrode system, for comparison. As expected, Figure 2(b) exhibits 30-fold higher current in the presence of redox cycling between ME and TE, *i.e.* comparing the GC-mode current between ME and TE to the non-GC current from ME alone. When ME and TE were used as working and quasi-reference electrodes in a

2-electrode configuration with no external electrode, Figure 2(c) shows approximately half of the GC current (*i.e.* ~14 times the non-GC current), which was obtained in the 4-electrode configuration. This agrees well with our previous report that the potential of TE, E_{TE}, tends to exhibit *zero* overpotential in the presence of excess SE when it is employed as a reference electrode.[27]

2.3. Voltage-Dependent Creation of Defect Channels in SiN_x Insulator

Next, we monitored GC mode current between ME and TE as a function of potential at BE, from E_{BE} = 0.5 V to 2.0 V in potential increments of 0.1 V. In these experiments, both ME and BE were used as working electrodes with TE as the reference electrode in a 3-electrode configuration. Figure S2(a) shows representative voltammograms of $Fe(CN)_6^{3/4-}$ obtained at ME with E_{BE} = 0.5 V, 1.0 V, 1.5 V, and 1.9 V, displaying almost identical current responses independent of E_{BE}. When BE was set to 2.0 V during the potential cycling of ME in the range ±0.4 V, the same current response was recorded in the forward scan from –0.4 V to +0.4 V, but on the reverse scan an abrupt change in current at both BE and ME was observed near +0.23 V, Figure S2(b). At this point the current at ME decayed to nearly background, while a small, but measurable, increase in BE current was observed simultaneously. This behavior is consistent with the formation of defect channels through the SiN_x, opening new mass transport pathways for $Fe(CN)_6^{3/4-}$ towards BE and producing an increased current response . Supporting this interpretation, a stochastic current burst was also observed from a newly prepared 3E-NEA upon applying a series of a potential-steps using BE and TE as working and reference electrodes, respectively, Figure S3. When E_{BE} was switched from 1.3 V to 2.0 V, the current at BE began to rise immediately from a non-conducting state and reached a maximum value ~1.0 μA at ~23s. In addition, stochastic current fluctuations were apparent, an observation which is discussed in detail below.

Once the abrupt current response was observed, E_{BE} was set back to +1.8 V, and the current response was monitored while scanning E_{ME}. Unexpectedly, as shown in **Figures 3**(a) and 3(b), the electrochemical current at ME was rectified after defect channels were formed in the SiN_x coating of BE. Redox cycling between ME and TE was still effective at positive potentials, but the cathodic current was decreased to less than half of its value before defect channel formation, yielding a rectification ratio, $R = 4.02$, calculated from the ratio of anodic to cathodic current at ±0.4 V, **Figures 3**(**b**) and **S4**.

2.4. Electrochemical Transistor Operation

After defect channels were introduced in the 70 nm SiN_x layer, CVs were repetitively obtained as a function of E_{BE}. When BE was left at OCP, effective redox cycling was established between ME and TE with little rectification ($R = 1.10$, Figure S5). ME maintained similar current response, as well as rectification ratio, in the potential range $-1.4\ V \leq E_{BE} \leq +1.6\ V$, **Figure 4**(a). However, the current began to deviate at $E_{BE} = +1.7$ V with an electrochemical rectification, $R = 1.65$, and rectification was further increased with increasing E_{BE}, Figures S6(a) and S6(c). Similarly, reverse rectification was observed starting at $E_{BE} = -1.5$ V and increasing with decreasing E_{BE}, as shown in Figures S6(b) and S6(d). Figure 4(a) summarizes the rectification ratio as a function of E_{BE} from −1.7 to 1.9 V. Note that negative values indicate negative electrochemical rectification obtained with negative E_{BE}. When BE was set at −1.7 and 1.9 V, the maximum electrochemical rectification was achieved as shown in Figures 4(b) and 4(c), $R = 61.8$ and −440 at $E_{BE} = +1.9$ and −1.7 V, respectively.

2.5. Current Dependence on E_{BE}

In order to understand the origin of the electrochemical rectification and its dependence on E_{BE}, we first performed cyclic voltammetry in supporting electrolyte (1 M KNO_3) only, using BE and TE as working and reference electrodes, respectively, without an external reference

electrode. Figure S7 shows no faradaic current is observed in 1 M KNO_3 solution. Under these conditions the only possible electrochemical reactions in the blank solution are water oxidation and reduction, neither of which exhibits measurable current in the potential window $|E| < 2$ V. 100 mM $Fe(CN)_6^{3/4-}$ was then added while sweeping the potential of BE relative to TE or ME in a 2-electrode configuration. Comparable current responses were recorded independent of reference electrode choice (ME or TE). This suggests negligible solution resistance along the current pathway associated with BE, solution, and ME or TE. Most of the potential likely drops at the surface of BE and/or along the defect channels in the SiN_x layer. In addition, *ca*. ±0.2 μA of reversible current caused by redox cycling of $Fe(CN)_6^{3/4-}$ was observed at E_{BE} = ~0 V. Since the redox cycling current between ME and TE in the 2-electrode configuration was ~20 μA in Figure 2(c), this suggests that the effective BE surface area was ~1% of the ME surface.

Naturally, the question arises as to the mechanism by which the defect channels are formed. The electric field required for dielectric breakdown of SiN_x is $\geq$ 0.4 V/nm.[29, 30] In these experiments, defect channels were observed to form at ~ 2 V, *i.e.*, or an electric field strength of ~0.03 V/nm, much lower than the threshold for dielectric breakdown measured over large areas. However, whenever E_{BE} exceeded a threshold value, a sudden increase in current was observed that was assigned to local breakdown, creating conducting channels filled with electrolyte solution. We hypothesize that structural defects or pinhole-like sites were formed during the deposition of the SiN_x, possibly correlated with the lack of an adhesion layer, *e.g.* Ti or Cr,[31] and these sites were susceptible to breakdown at lower electric fields than the canonical value, thus leading to formation of defect channels. In addition, in negative control experiments, I-V measurements conducted before defect channel creation showed only capacitive current between BE-ME and ME-TE, demonstrating no leakage current between the electrodes with an intact 70 nm SiN_x.

In addition to the $Fe(CN)_6^{3/4-}$ redox cycling current at ~0 V, strong irreversible waves were observed at E_{BE} = ±1.7 V. The observed two-step current response was reproducible over several potential scans of BE in a range of ±2 V, suggesting that, once formed, the physical structure of the SiN_x layer, including the defect channels, was stable. Supporting this interpretation, Figure S8 shows a cross-sectional SEM image of the BE/SiN_x architecture after formation of defect channels. There is no noticeable difference compared to the image before the defect channel formation in the SiN_x, *cf.* Figure 1, indicating that either the defect channels were below resolution limit of the SEM, or the cross-section did not intersect any defects. Thus, both the BE redox cycling current magnitude (~1% of the ME/TE current) and the SEM cross-sectional image indicate that most of the BE surface remained covered by SiN_x even after the abrupt current spikes were measured from BE. Taken together these observations support the production of small defect channels, which we suggest are ≤ 10 nm in diameter.

2.6. Voltage-Dependent Mass Transport

To characterize the nature of the irreversible current wave at $|E_{BE}| \geq 1.7$ V, we performed chronoamperometry with multiple potential steps at E_{BE} = +0.4, +0.8, +1.3, and +2.0 V. After defect channels were introduced in the SiN_x layer, the array was air-dried overnight to reduce moisture inside the channels. **Figure 5** shows current-time data acquired after the application of multiple sequential potential steps. As E_{BE} increases from +0.4 V to +1.3 V, the current also increased in steps. The current measured at E_{BE} = 1.3 V, *i.e.* ~0.2 μA, is very similar to the reversible current at E_{BE} = ~0 V exhibited in Figure S7, indicating that the current mainly results from redox cycling under these conditions. However, when E_{BE} was further increased to +2.0 V, a current burst with strong fluctuations was observed, which is similar to Figure S3, suggesting that it reflects defect channel properties. Furthermore, the current dynamics at t > 30 s are characterized by two principal features: (1) a stable current floor, capable of

undergoing abrupt changes, *e.g.* at $t \sim 54$ s; and (2) a strongly fluctuating current with the magnitude of the fluctuations decreasing over time. Both features reflect the detailed structure of, and dynamics within, the defect channels.

First, the dynamic fluctuations are qualitatively similar to the current behavior resulting from the electric-field-induced wetting/dewetting of nanochannels owing to simultaneous condensation and evaporation of water.[18] Jiang and coworkers demonstrated that water transport was dual-gated by electrostatic charge and/or electric-field in 12 μm thick polyethylene terephthalate (PET) with nanopore diameters 3 nm < d < 40 nm.[32] In contrast to the electric-field-induced wetting of hydrophobic nanopores, *e.g.* carbon nanotubes, which is capable of being effectively gated in pores as large as 100 nm,[17] the electrostatically charged PET nanopores must be smaller than 10 nm to exhibit successful gating. These observations suggest that the irreversible increase in current at $|E_{BE}| \geq 1.7$ V originates from electric-field-induced wetting and dewetting in the defect channels, thereby producing dynamic current fluctuations with time. In addition, the stable current floor suggests the presence of larger defect channels that are not susceptible to electric field wetting/dewetting, remaining open to stable transport over longer times, before closing abruptly. Over time, after running several (≥ 5) sequential potential-step measurement programs, the current stabilized and showed a typical diffusion-controlled current at E_{BE} = +2.0 V, **Figure S9**. Stable current behavior was also obtained when a constant voltage to BE was applied for sufficiently long. This Cottrell current behavior confirms that, aside from the defect channels, the leakage current through the SiN_x film is negligible.

To summarize, the current behavior shown in Figure 5 at $t > 30$ s likely arises from different types of defect channels through the bottom SiN_x, created when E_{BE} was held at +2.0 V *vs.* TE. The reversible current at E_{BE} = ~0 V as well as the current floor at longer times at +2.0 V

can be explained by larger defect channels which are continuously filled with aqueous solution regardless of E_{BE}. In addition, there are smaller defect channels that can undergo wetting/dewetting transitions that alter the defect channel filling. For example, the non-wetted state can be switched to a wetted state by exceeding the threshold potential, *i.e.* $E_{BE} = \pm 1.7$ V, giving rise to an irreversible current increase.

2.7. Current Pathway for Electrochemical Transistor Operation

We further increased the magnitude of E_{BE} to either +2.2 V or –1.95 V *vs*. TE, beyond the threshold values for the electric-field-induced wetting, in order to examine whether electrochemical rectification ratio was altered. Interestingly, rectification at BE was diminished with greatly suppressed cathodic and anodic currents, respectively, Figure S10. However, E_{BE}-controlled electrochemical rectification behavior was readily retrieved at ME over the potential range -0.8 V < E_{ME} < +0.8 V, **Figure 6**. Current measured at BE remained relatively constant when E_{BE} was set to either +2.2 V or –1.95 V, indicating that the defect channels across the SiN_x layer are maintained above the threshold value for electric-field-induced wetting.

It is noteworthy that Figure S10(a) exhibits current fluctuations recorded from both ME and BE. The concurrent nature of these fluctuations suggests that BE and ME are electrochemically coupled such that, when they are set to opposite potentials for the oxidation and reduction of $Fe(CN)_6^{3/4-}$, and when the defect channels are maintained in the wet state, current from ME flows towards BE rather than TE. This is also evident in Figures S6(a) and S6(c). When ME and BE were set to the same potential polarity against TE, *e.g.* both for oxidation of $Fe(CN)_6^{4-}$, ME showed effective anodic current resulting from redox cycling phenomenon between ME and TE. However, significantly suppressed cathodic current was observed from ME when E_{ME} was poised at negative potentials, while BE was held at a

positive potential. Under these conditions, *i.e.* positive BE and negative ME, the system is poised for redox cycling of $Fe(CN)_6^{3/4-}$, but with the majority of the current passing between ME-BE, rather than ME-TE. The apparent rectification then arises from the limited mass transport between ME and BE provided by the nanochannels in the SiN_x. Analogous, but oppositely polarized rectification behavior is obtained when E_{BE} is poised at strongly negative potentials for reduction of $Fe(CN)_6^{3-}$.

In support of this interpretation, the limited mass transport pathways between ME and BE generated strong electrochemical rectification, as shown in **Figures S11**(**a**) and (**b**). In contrast, ME produced no electrochemical rectification when all three electrodes (in ring-ring-disk configuration) were directly exposed to the electrolyte solution, **Figure S11**(**c**). In the complete absence of the 70 nm SiN_x dielectric layer, BE can participate in redox-cycling based current amplification, so ME can collect redox cycling current from both TE and BE. For instance, with E_{BE} = +0.4 V relative to TE in **Figure S11**(**a**), E_{ME} = –0.4 V collected the redox cycling current both from TE (*ca*. –40 μA) and BE (*ca*. –20 μA), yielding –60 μA in total. On the other hand, when E_{ME} = +0.4 V, *ca*. 40 μA was collected from TE only. In a similar manner, reversed current behavior was observed at ME and BE when E_{BE} was set to –0.4 V relative to TE, as shown in **Figure S11**(**b**). These collective control experiments in the absence of a SiN_x layer on BE strongly support the interpretation that the defect channel-mediated mass transport between ME and BE is directly responsible for electrochemical transistor action upon electric-field-induced wetting/dewetting of defect nanochannels.

3. Conclusion

Efficient electrochemical transistor action is realized here by combining a number of features and capabilities of 3E-NEAs. Like their 2E-NEA relatives, these structures support strong redox cycling between the nanopore-housed TE and ME when E_{BE} is maintained at potentials

$|E_{BE}| < 1.7$V. However, potentials $|E_{BE}| > 1.7$ V are accompanied by an abrupt change in amperometric behavior at BE, indicating the formation of new current pathways that we interpret in terms of voltage-induced defect channels in the SiN_x layer insulating BE from the bulk of the nanopore. These defect channels, in turn, give rise to two interesting phenomena: electric-field-induced wetting and dewetting as well as voltage-controlled current pathway regulation. The defect channels created in the SiN_x layer are responsible for transport of $Fe(CN)_6^{3/4-}$ towards/from BE, as illustrated by two distinct levels of current: reversible redox cycling current at $E_{BE} = \sim 0$ V *vs*. TE and more dominantly, irreversible current at $|E_{BE}| > 1.7$ V. The larger defect channels stay in the wet state continuously, independent of E_{BE}, contributing to the reversible redox cycling current. The smaller defect channels, however, can be switched between wet and dry states, by electric-field-induced wetting and dewetting. Once the electric field across the defect channels overcomes the threshold value, condensation of water inside the channels dominates water evaporation, thereby opening more transport pathways to BE. In addition, when the defect channels are switched to the wet state by setting E_{BE} beyond the threshold potential, electrochemical transistor function can be realized. When ME and BE exhibit the same potential polarity relative to the formal potential, $E^{0\prime}$, efficient redox cycling current is observed between ME and TE. However, when BE and ME are oppositely biased relative to E^0, only negligible current is observed from ME, because the dominant current pathway switches from ME-TE to ME-BE, resulting in transistor operation.

The electric-field-induced wetting-based electrochemical transistors developed in this work represent a new architecture for controlling transport and coupled electrochemical reactivity in nanopore electrode arrays. In addition, they hold substantial promise for devising advanced iontronic devices, which are relevant to applications ranging from drug delivery to molecular separations to water purification.

4. Experimental Section

Chemicals and Materials: Potassium ferrocyanide ($K_4Fe(CN)_6$), potassium ferricyanide ($K_3Fe(CN)_6$), potassium nitrate (KNO_3), and polystyrene latex beads (0.46 μm in mean diameter) were obtained from Sigma-Aldrich (USA) and used as received. All aqueous solutions used for electrochemical analysis were prepared with deionized water ($\rho \sim 18.2$ MΩ cm, Millipore Milli-Q system).

Electrochemical Measurements: Unless otherwise indicated, all electrochemical measurements were performed with 100 mM $Fe(CN)_6^{3/4-}$ in 1 M KNO_3 (pH 8.6) composed of equal concentration of reduced and oxidized species using a CHI842A electrochemical workstation (CH Instruments, USA). Non-GC operation was conducted in 3-electrode system, in which one of the 3 Au layers was employed as working electrode with a Pt wire counter electrode and a Ag/AgCl reference electrode (Harvard Apparatus, USA). For GC-mode operation, either 4-or 2-electrode system was used. In the 4-electrode system, two Au electrodes (*e.g.*, ME and TE) were chosen as 1st and 2nd working electrodes with Pt counter and Ag/AgCl reference electrodes. Otherwise, BE or ME and TE were used as working and reference/counter electrodes, respectively, in the 2-electrode system without any external electrode. In order to observe electrochemical transistor operation, both ME and BE were used as working electrodes relative to a TE reference electrode in a 3-electrode configuration without any external electrode. All voltammetric responses were obtained with a scan rate of 0.1 V s^{-1} and a sampling rate of 10 Hz. For current-time measurements with multiple potential steps, BE and TE were employed as working and reference electrodes in the 2-electrode configuration. In order to faithfully capture changes in current, the sampling frequency was set at 5 kHz, which is the maximum capacity of the potentiostat.

Supporting Information
Supporting Information is available from the Wiley Online Library or from the author.

Acknowledgements

The work described here was supported by the Department of Energy Office of Science through grant DE FG02 07ER15851 (S-RK) and by the National Science Foundation grant CHE 1904196 (SB, KF). The authors acknowledge the expert assistance of staff at the Notre Dame Integrated Imaging Facility and the Notre Dame Nanofabrication Facility in the preparation and characterization of the nanostructures used in these studies.

Received: ((will be filled in by the editorial staff))
Revised: ((will be filled in by the editorial staff))
Published online: ((will be filled in by the editorial staff))

References

[1] D. W. M. Arrigan, *Analyst* **2004**, *129*, 1157.

[2] S. G. Lemay, *ACS Nano* **2009**, *3*, 775.

[3] S. W. Kowalczyk, T. R. Blosser, C. Dekker, *Trends Biotechnol.* **2011**, *29*, 607.

[4] X. Hou, H. Zhang, L. Jiang, *Angew. Chem. Int. Ed.* **2012**, *51*, 5296.

[5] B. N. Miles, A. P. Ivanov, K. A. Wilson, F. Doğan, D. Japrung, J. B. Edel, *Chem. Soc. Rev.* **2013**, *42*, 15.

[6] K. J. Krause, E. Kätelhön, S. G. Lemay, R. G. Compton, B. Wolfrum, *Analyst* **2014**, *139*, 5499.

[7] H. Chun, T. D. Chung, *Annu. Rev. Anal. Chem.* **2015**, *8*, 441.

[8] W. Shi, A. K. Friedman, L. A. Baker, *Anal. Chem.* **2017**, *89*, 157.

[9] R. Gao, Y.-L. Ying, Y.-J. Li, Y.-X. Hu, R.-J. Yu, Y. Lin, Y.-T. Long, *Angew. Chem. Int. Ed.* **2018**, *57*, 1011.

[10] Y.-L. Ying, R. Gao, Y.-X. Hu, Y.-T. Long, *Small Methods* **2018**, *2*, 1700390.

[11] M. Barboiu, A. Gilles, *Acc. Chem. Res.* **2013**, *46*, 2814.

[12] C. Neale, N. Chakrabarti, P. Pomorski, E. F. Pai, R. Pomès, *PLoS Comput. Biol.* **2015**, *11*, e1004303.

[13] O. Beckstein, M. S. P. Sansom, *Phys. Biol.* **2006**, *3*, 147.

[14] M. Ø. Jensen, D. W. Borhani, K. Lindorff-Larsen, P. Maragakis, V. Jogini, M. P. Eastwood, R. O. Dror, D. E. Shaw, *Proc. Natl. Acad. Sci. U. S. A.* **2010**, *107*, 5833.

[15] A. Anishkin, S. Sukharev, *Biophys. J.* **2004**, *86*, 2883.

[16] S. Smirnov, I. Vlassiouk, P. Takmakov, F. Rios, *ACS Nano* **2010**, *4*, 5069.

[17] S. N. Smirnov, I. V. Vlassiouk, N. V. Lavrik, *ACS Nano* **2011**, *5*, 7453.

[18] M. R. Powell, L. Cleary, M. Davenport, K. J. Shea, Z. S. Siwy, *Nat. Nanotechnol.* **2011**, *6*, 798.

[19] G. Xie, P. Li, Z. Zhao, Z. Zhu, X.-Y. Kong, Z. Zhang, K. Xiao, L. Wen, L. Jiang, *J. Am. Chem. Soc.* **2018**, *140*, 4552.

[20] Q. Chen, K. McKelvey, M. A. Edwards, H. S. White, *J. Phys. Chem. C* **2016**, *120*, 17251.

[21] M. A. G. Zevenbergen, B. L. Wolfrum, E. D. Goluch, P. S. Singh, S. G. Lemay, *J. Am. Chem. Soc.* **2009**, *131*, 11471.

[22] J. Xiong, Q. Chen, M. A. Edwards, H. S. White, *ACS Nano* **2015**, *9*, 8520.

[23] Y. Fan, T. J. Anderson, B. Zhang, *Curr. Opin. Electrochem.* **2018**, *7*, 81.

[24] H. S. White, K. McKelvey, *Curr. Opin. Electrochem.* **2018**, *7*, 48.

[25] C. Ma, N. M. Contento, P. W. Bohn, *J. Am. Chem. Soc.* **2014**, *136*, 7225.

[26] K. Fu, D. Han, S.-R. Kwon, P. W. Bohn, *ACS Nano* **2018**, *12*, 9177.

[27] S.-R. Kwon, K. Fu, D. Han, P. W. Bohn, *ACS Nano* **2018**, *12*, 12923.

[28] C. Ma, N. M. Contento, L. R. Gibson, P. W. Bohn, *ACS Nano* **2013**, *7*, 5483.

[29] S. M. Sze, *J. Appl. Phys.* **1967**, *38*, 2951.

[30] H. Kwok, K. Briggs, V. Tabard-Cossa, *PLoS One* **2014**, *9*, e92880.

[31] J. Vancea, G. Reiss, F. Schneider, K. Bauer, H. Hoffmann, *Surf. Sci.* **1989**, *218*, 108.

[32] K. Xiao, Y. Zhou, X.-Y. Kong, G. Xie, P. Li, Z. Zhang, L. Wen, L. Jiang, *ACS Nano* **2016**, *10*, 9703.

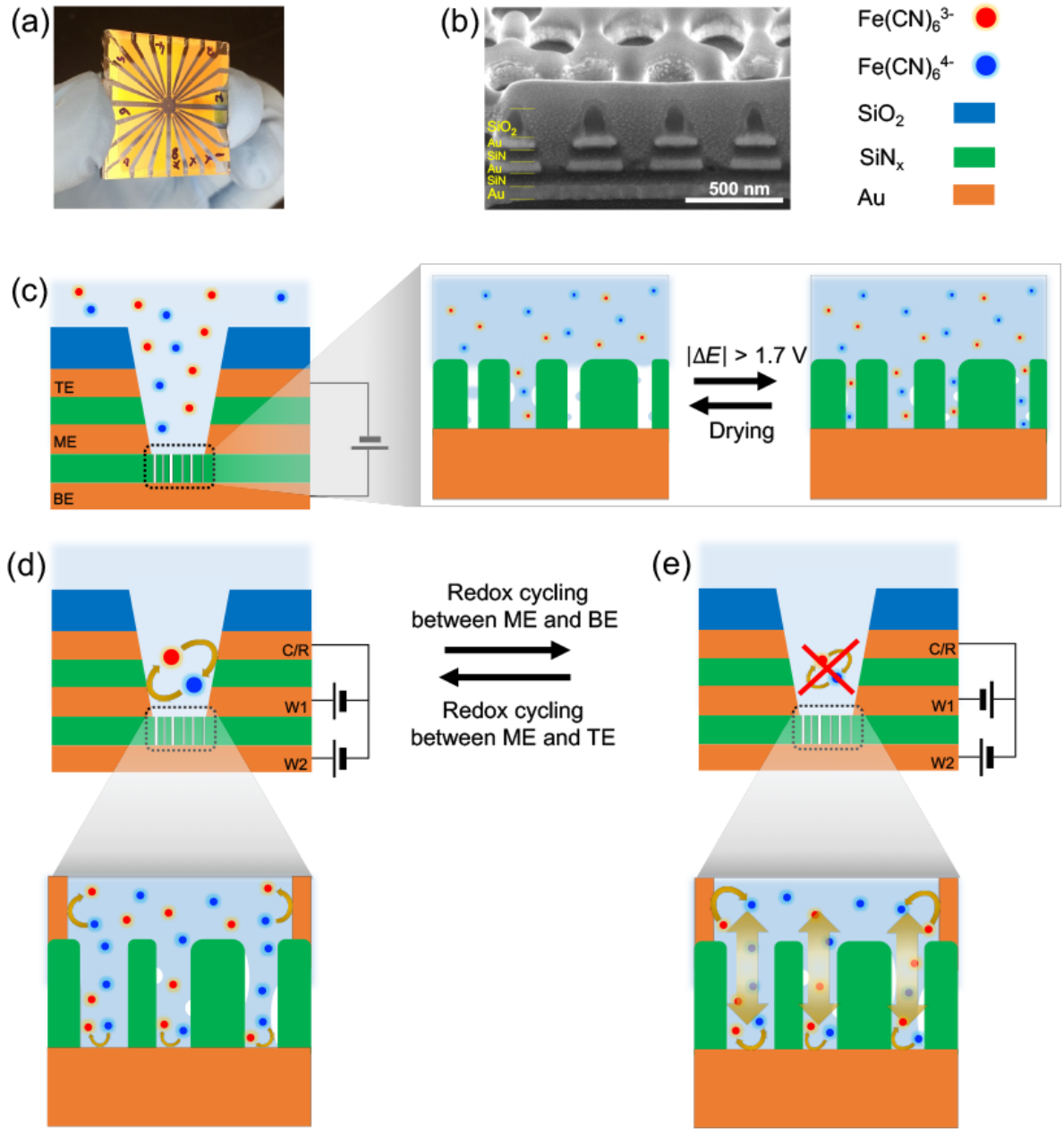

Figure 1. (a) Photograph of fabricated a 3E-NEA device composed of 8 independent arrays. (b) Cross-sectional SEM image showing individual nanopore structure. The bottom Au electrode (BE) is covered by a 70 nm thick layer of SiN_x, whereas the middle and top Au electrodes (ME and TE) are in direct contact with the nanopore-confined solution. Pt metal was deposited over the nanopores before cross-sectional imaging for clear structural observation. (c) Schematic illustration of the nanopore showing electric-field-induced wetting and dewetting of the defect channels in the SiN_x. (d,e) Efficient redox cycling occurs between ME and TE when the potential of ME and BE are both set for electrochemical oxidation of

$Fe(CN)_6^{3/4-}$ relative to its formal potential (d), but when the potential of ME is biased opposite to BE, then redox cycling is established between ME and BE, and its magnitude is limited by the need to transport redox species across the defect channels, as indicated by the broad arrows (e).

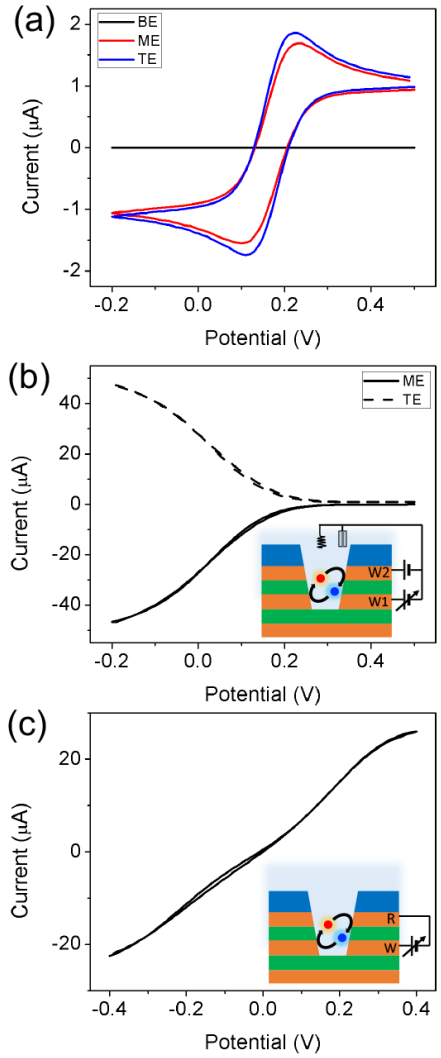

Figure 2. Voltammograms of 100 mM $Fe(CN)_6^{3/4-}$ in 1 M KNO_3. (a) Non-GC voltammograms obtained in a 3-electrode system, where one of the Au layers was used as the working electrode with external Pt counter and Ag/AgCl reference electrodes, while holding the other 2 electrodes at OCP. (b) GC mode operation, in which ME was swept between +0.5 and –0.2 V, whereas TE was held at +0.5 V with Ag/AgCl reference and Pt counter electrode in a 4-electrode system. (c) Voltammograms obtained from ME working and TE reference electrodes in a 2-electrode system without any external counter/reference electrode. All voltammograms were obtained with a scan rate of 0.1 V s^{-1} and a sampling rate of 10 Hz.

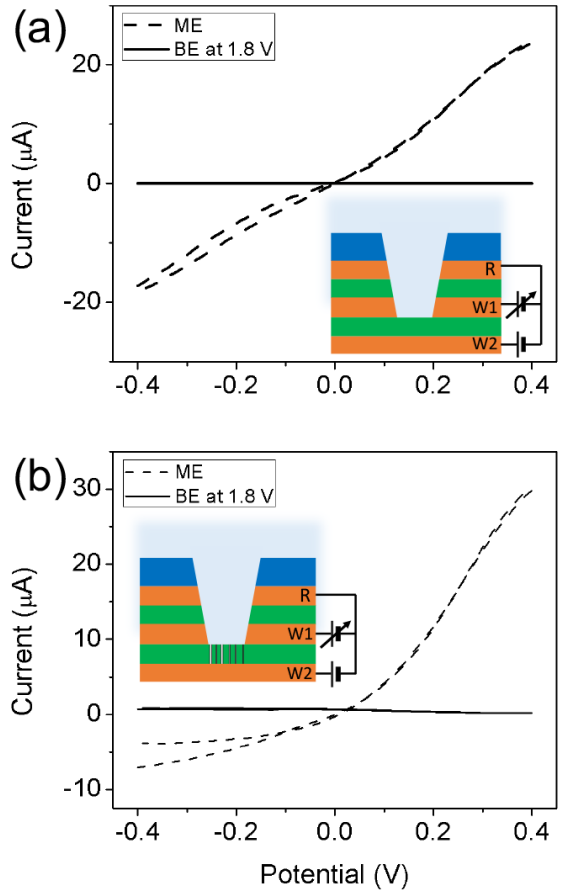

Figure 3. Voltammograms of 100 mM $Fe(CN)_6^{3/4-}$ in 1 M KNO_3 before (a) and after (b) formation of defect channels through the 70nm-SiN_x layer. BE was set to 1.8 V while scanning ME in a potential range of ±0.4 V relative to TE in a 3-electrode configuration, *i.e.* ME and BE were working electrodes with TE as reference electrode.

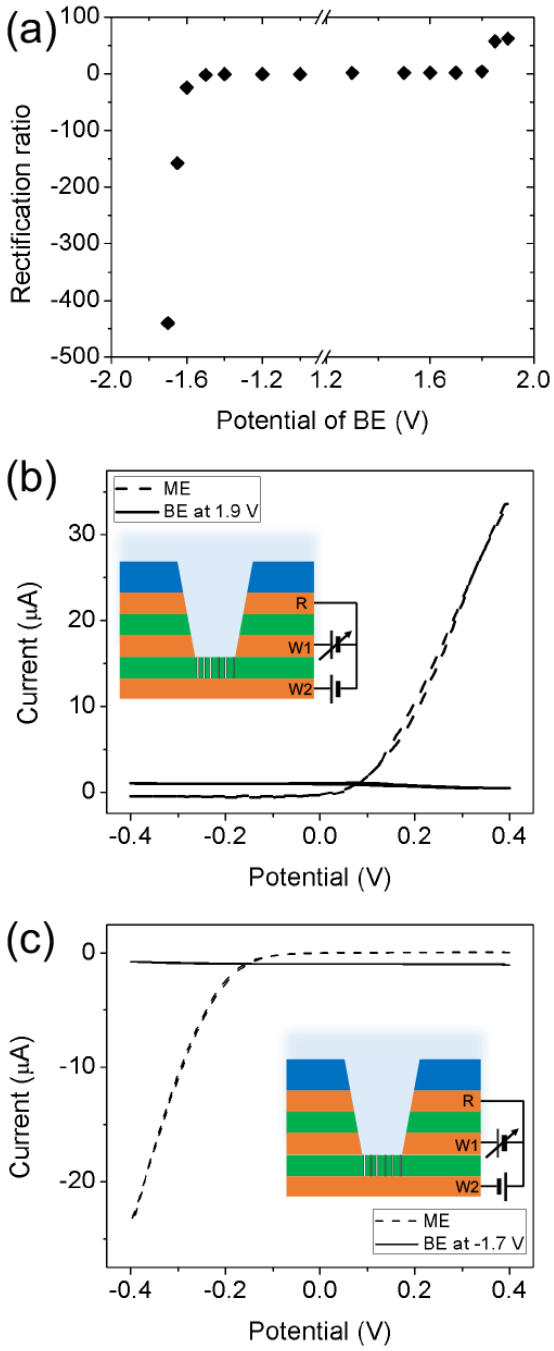

Figure 4. (a) Rectification ratio as a function of E_{BE} obtained from voltammograms of 100 mM $Fe(CN)_6^{3/4-}$ in 1 M KNO_3. In order to denote the polarity dependence of electrochemical rectification, the negative sign is introduced for negative values of E_{BE}. (b,c) Representative voltammograms using 3-electrode configuration, in which ME was scanned in the range ±0.4 V and BE was held at +1.9 V (b) or –1.7 V (c) relative to TE.

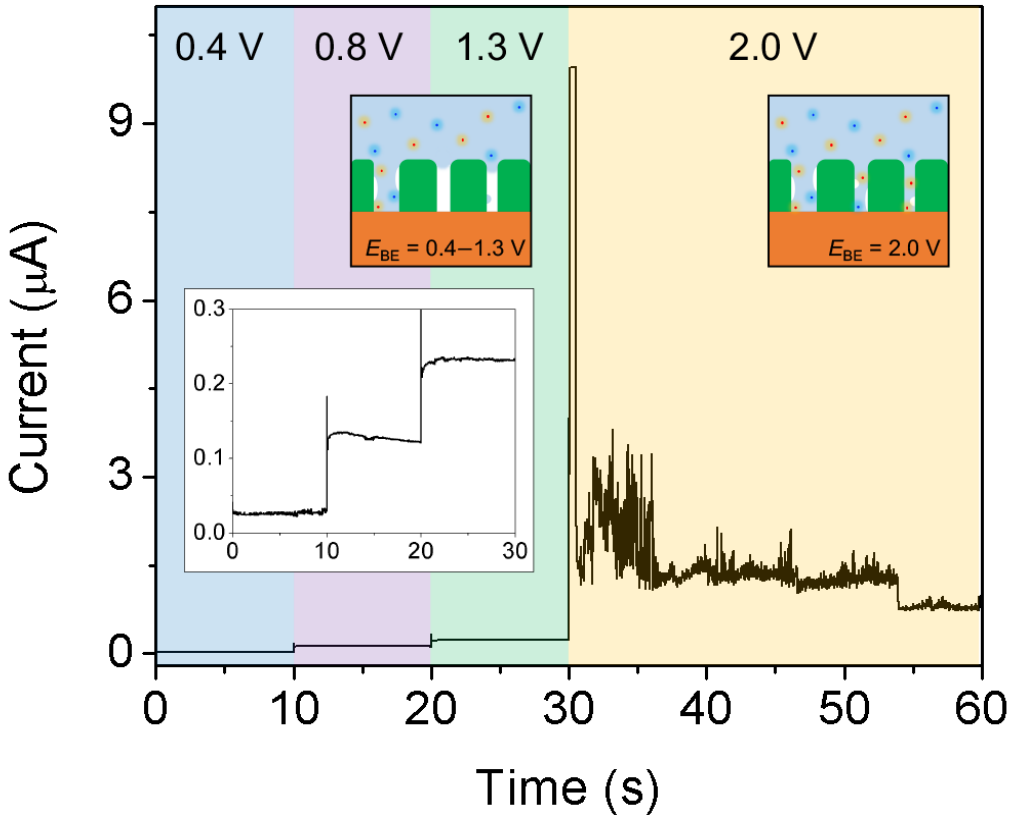

Figure 5. Current-time measurements with multiple potential steps, E_{BE} = 0.4 V, 0.8 V, 1.3 V, and 2.0 V relative to TE in the 2-electrode configuration. (*Inset*) Enlarged trace from 0 to 30 s. Current sampling rate was set at the maximum capacity of the potentiostat, 5 kHz.

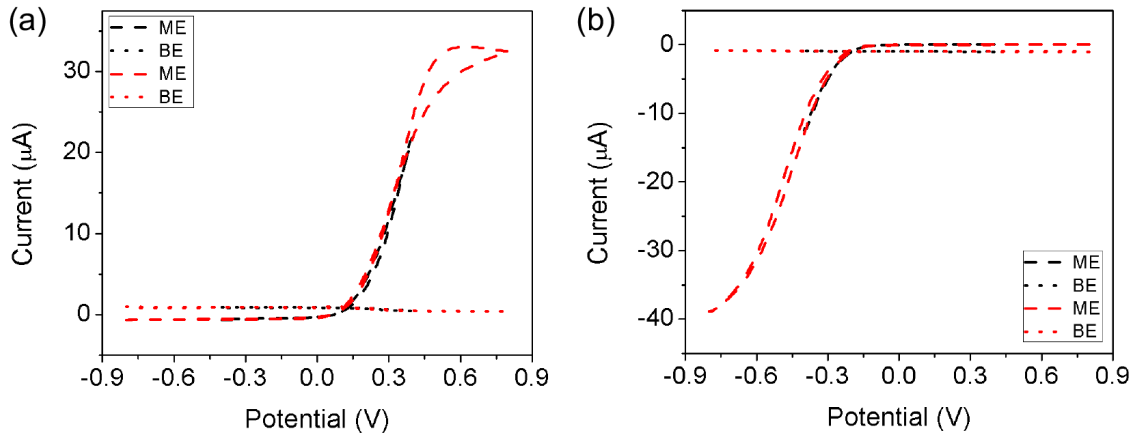

Figure 6. Voltammograms of 100 mM $Fe(CN)_6^{3/4-}$ in 1 M KNO_3 at E_{BE} = +2.0 V (a) or –1.8 V (b) while ME was scanned in a range of potential either ±0.4 V (black) or ±0.8 V (red) against TE in 3-electrode configuration.

Electrowetting-mediated transistor action is realized using triple-electrode-embedded nanopore arrays, in which middle and top electrodes are in direct contact with electrolyte solution while bottom electrode is partially and temporarily accessible to the solution through defect nanochannels in silicon nitride layer. Upon electric-field-induced wetting of the defect nanochannels, electrochemical rectification is obtained depending on the potential of bottom electrode relative to the middle electrode.

Keyword
Electrochemical transistors, electrowetting, gating, nanochannels, nanopores

Seung-Ryong Kwon, Seol Baek, Kaiyu Fu, and Paul W. Bohn*

Electrowetting-Mediated Transport to Produce Electrochemical Transistor Action in Nanopore Electrode Arrays

ToC figure

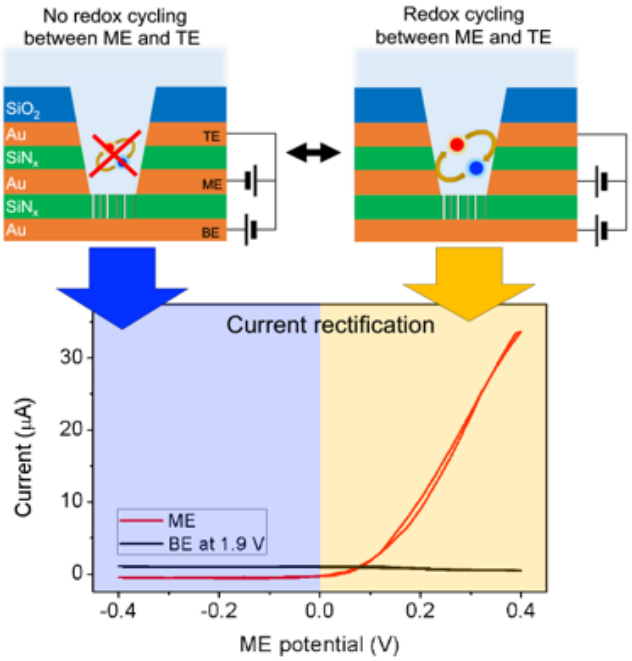

Supporting Information

Electrowetting-Mediated Transport to Produce Electrochemical Transistor Action in Nanopore Electrode Arrays

*Seung-Ryong Kwon, Seol Baek, Kaiyu Fu, and Paul W. Bohn**

Device Fabrication and Characterization: Triple-embedded NEAs (3E-NEAs) were fabricated by adapting a previous method used to prepare dual-embedded NEAs.[1, 2] Briefly, each gold electrode (*i.e.* 100 nm for BE and and 70 nm for ME and TE,) was lithographically patterned on a pre-cleaned glass slide (Glass D, Applied Microarrays, Inc.). A 70 nm thick SiN_x layer was deposited by electron-beam evaporation between the gold layers for electrical insulation and lastly, 200 nm of SiO_2 was deposited as the outmost layer to insulate the NEA and to facilitate aqueous solution filling into the nanopore arrays. After thin film deposition and patterning, a monolayer of polystyrene latex beads (d ~ 460 nm) was formed at an air-liquid interface and carefully transferred onto the glass substrate. After the bead diameter was reduced to ~250 nm by an oxygen-plasma treatment, a chrome mask was deposited, and then the polystyrene beads were removed from the substrate in acetone solution. Next, a square pattern of 100 × 100 μm^2 was lithographically opened to limit the area of the NEA to the region where the three electrodes overlapped, Figure 1(a). Finally, the nanopore structures were produced using multistep reactive-ion etching (Plasmatherm 790) until the ring structure of ME was developed. Then, the remaining photoresist was removed from the surface by immersing in acetone solution. SEM images were obtained using a FEI-Helios Dual Beam FIB at an accelerating voltage of 5 kV and a beam current of 86 pA. For cross-sectional imaging of the NEAs, Pt metal was pre-deposited over the region of interest to protect the

nanoporous structure as well as to provide clear cross-sectional imaging contrast. Then, the NEA substrate was tilted at 52 degrees and gradually sliced with a focused ion beam until a cross-sectional nanopore structure was obtained.

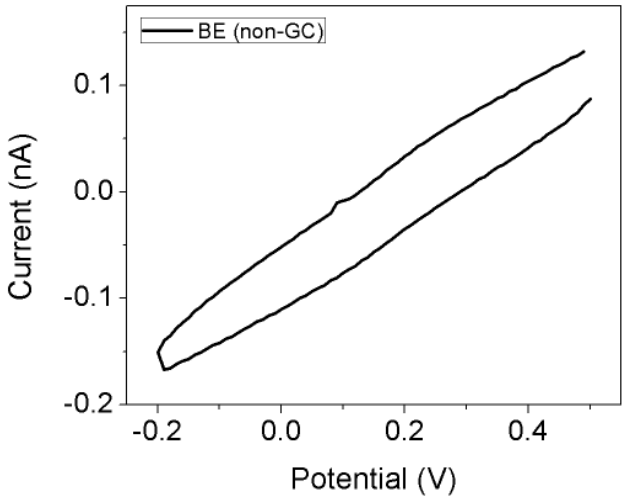

Figure S1. Voltammetric response of 100 mM $Fe(CN)_6^{3/4-}$ in 1 M KNO_3. BE was used as working electrode with external Pt counter and Ag/AgCl reference electrodes in a 3-electrode configuration. The other 2 Au electrodes, *i.e.* TE and ME, were left at open-circuit potential during the measurement.

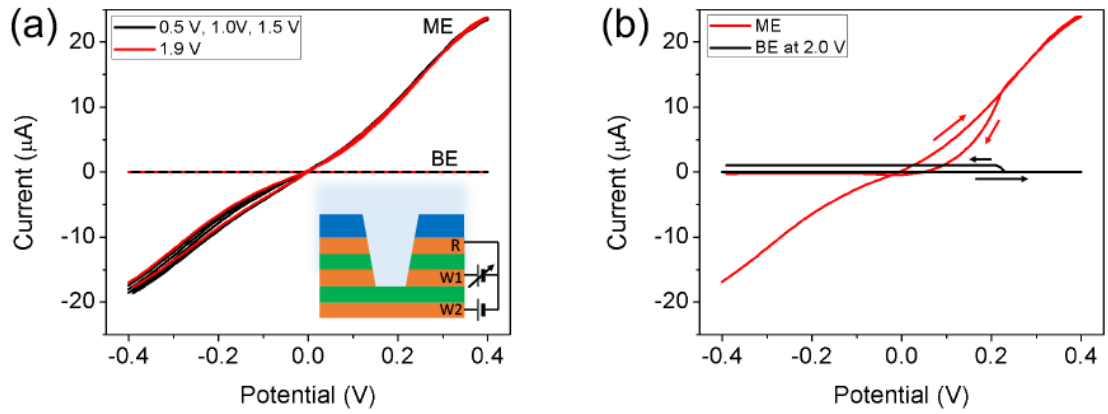

Figure S2. Representative voltammograms of 100 mM $Fe(CN)_6^{3/4-}$ in 1 M KNO_3 as a function of E_{BE}, with E_{BE} = 0.5 V, 1.0 V, 1.5 V, and 1.9 V (a), and 2 V (b). In each CV E_{ME} was scanned from –0.4 V to +0.4 V relative to TE. The detailed time course of the 2V experiment is indicated by arrows in panel (b). Note that in this experiment, voltammetric responses were monitored from 0.5 V to 2.0 V relative to TE with a potential step of 0.1 V increment.

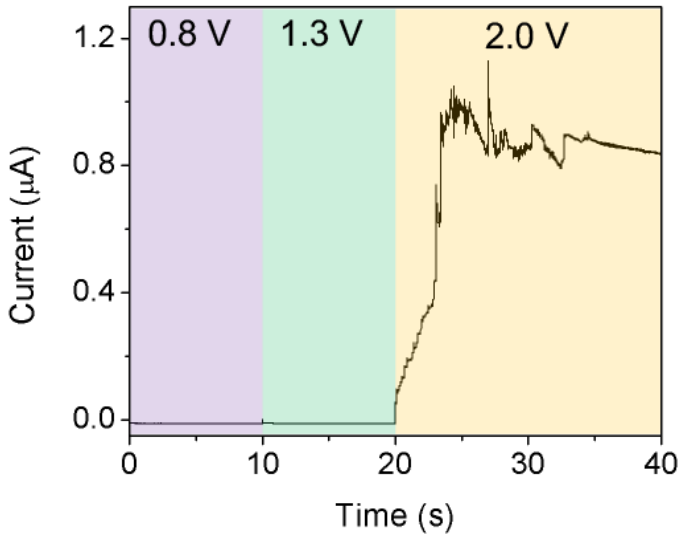

Figure S3. Multiple potential step current-time trace at E_{BE} = 0.8, 1.3, and 2.0 V *vs*. TE. ME was left at OCP in the experiment and sampling frequency was 5 kHz.

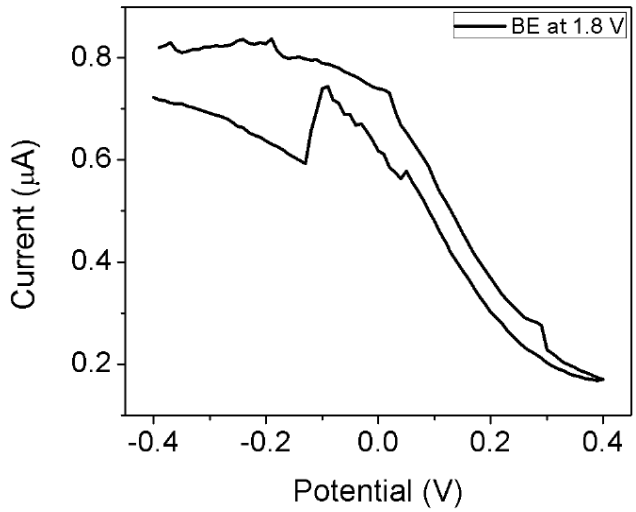

Figure S4. Enlarged voltammogram of 100 mM $Fe(CN)_6^{3/4-}$ in 1 M KNO_3 from Figure 3(b) showing the current response for BE only.

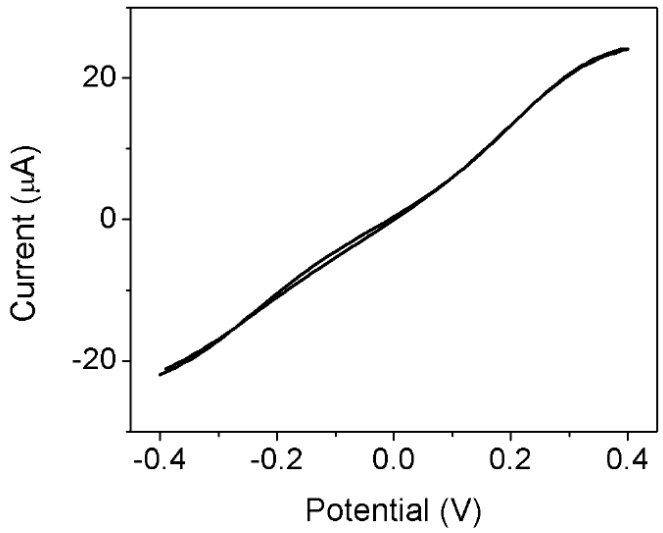

Figure S5. Voltammogram of 100 mM $Fe(CN)_6^{3/4-}$ in 1 M KNO_3 obtained after creating nanochannels through the SiN_x. ME was swept between ±0.4 V relative to TE in 2-electrode configuration, while BE was left at OCP.

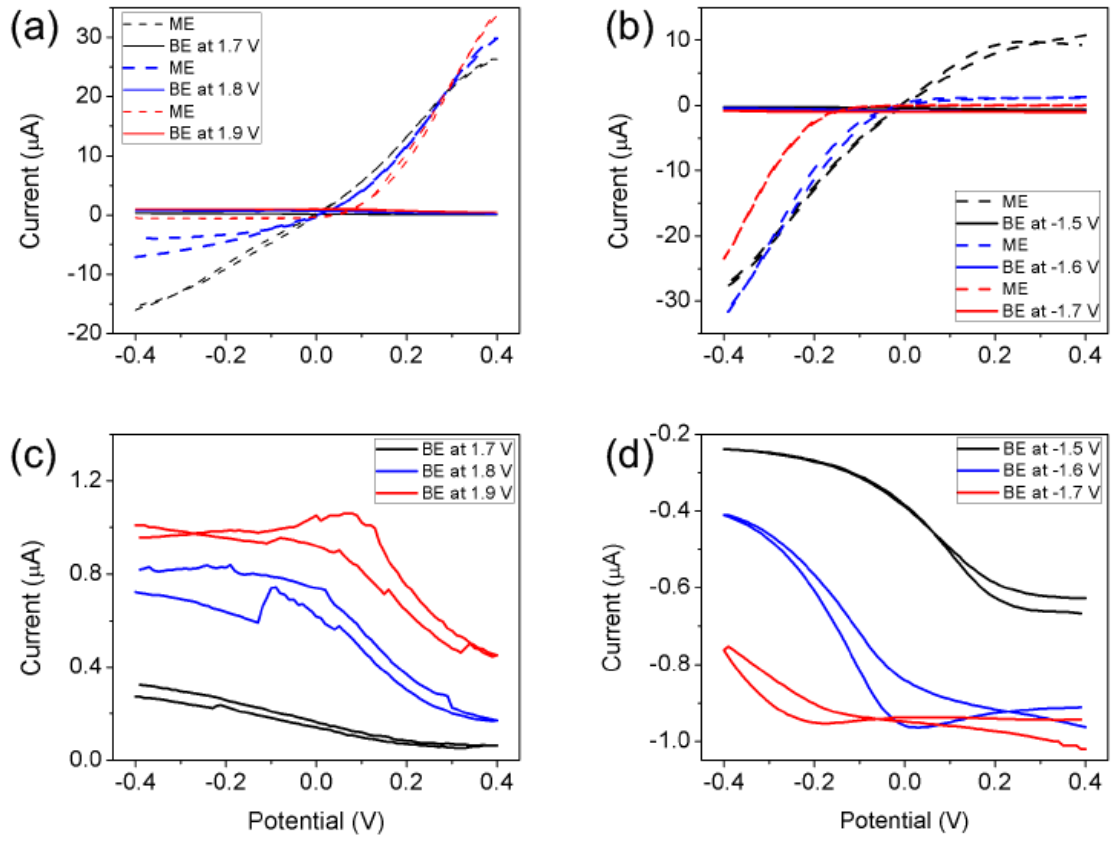

Figure S6. Voltammogram of 100 mM $Fe(CN)_6^{3/4-}$ in 1 M KNO_3 as a function of E_{BE} at 1.7, 1.8, 1.9 V (a,c) and −1.5, −1.6, −1.7 V (b,d) while scanning ME in a potential range of ±0.4 V: (a,b) full range of voltammograms for ME and BE; (c,d) magnified voltammograms for BE only. Both ME and BE were used as working electrodes and TE was used as the reference electrode in 3-electrode system.

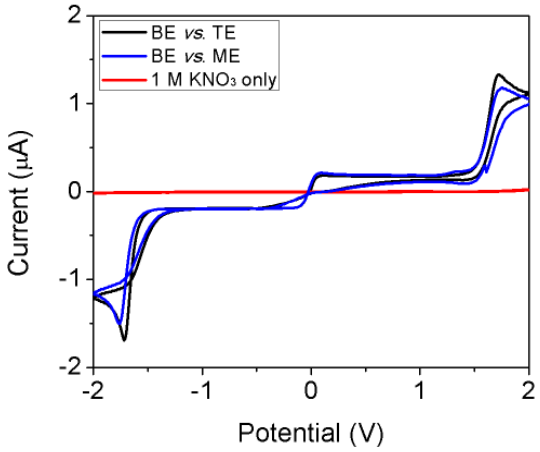

Figure S7. Voltammograms of 100 mM $Fe(CN)_6^{3/4-}$ in 1 M KNO_3 (blue, black) and 1 M KNO_3 only (red) using 2-electrode configuration, in which BE was employed as working electrode and ME (blue) or TE (black, red) as reference electrode.

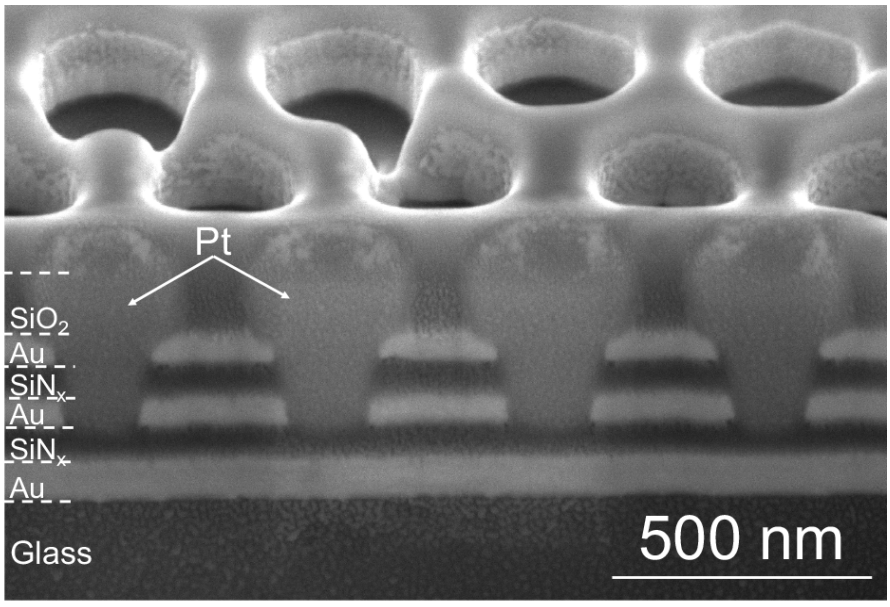

Figure S8. A cross-sectional SEM image showing the detailed nanopore structure including apparently well-preserved structure of the bottom SiN_x onto the bottom Au layer after defect channel creation in a strong electric-field (*e.g.* 2 V *vs*. TE). Pt metal was deposited over the nanopores before cross-sectional imaging for clear structural observation.

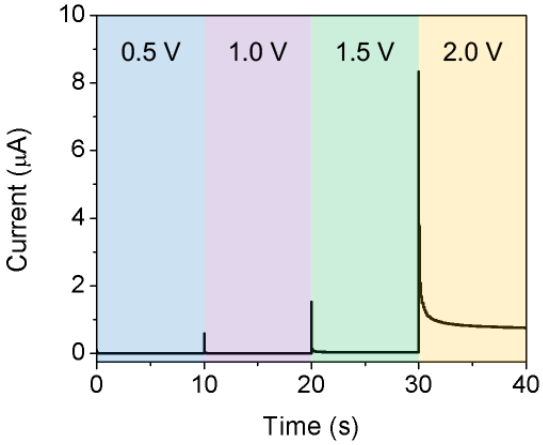

Figure S9. Amperometric response after multiple potential steps at E_{BE} = +0.5 V, +1.0 V, +1.5 V, and +2.0 V relative to TE. This current-time trace was obtained after the current response stabilized, showing no fluctuation after several measurement sequences at a sampling rate of 5 kHz.

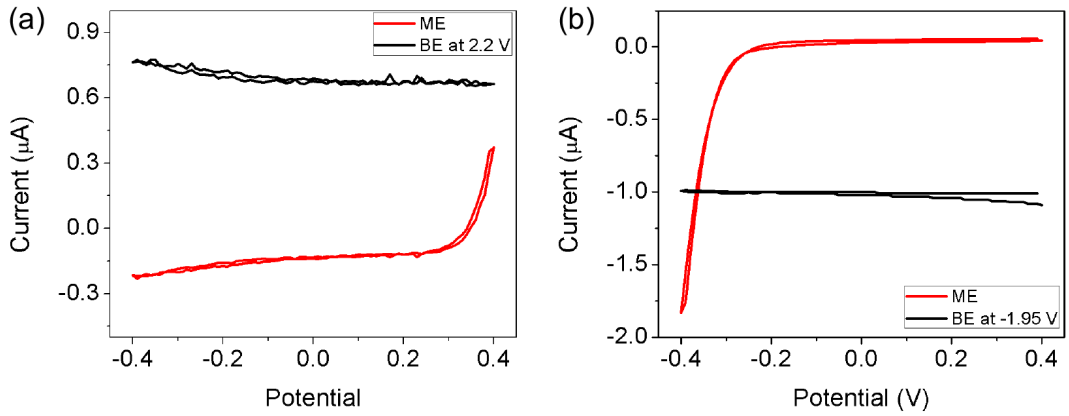

Figure S10. Voltammograms of 100 mM $Fe(CN)_6^{3/4-}$ in 1 M KNO_3 at E_{BE} = +2.2 V (a) and −1.95 V (b) during the potential scanning of ME (±0.4 V) relative to TE as reference in 3-electrode configuration.

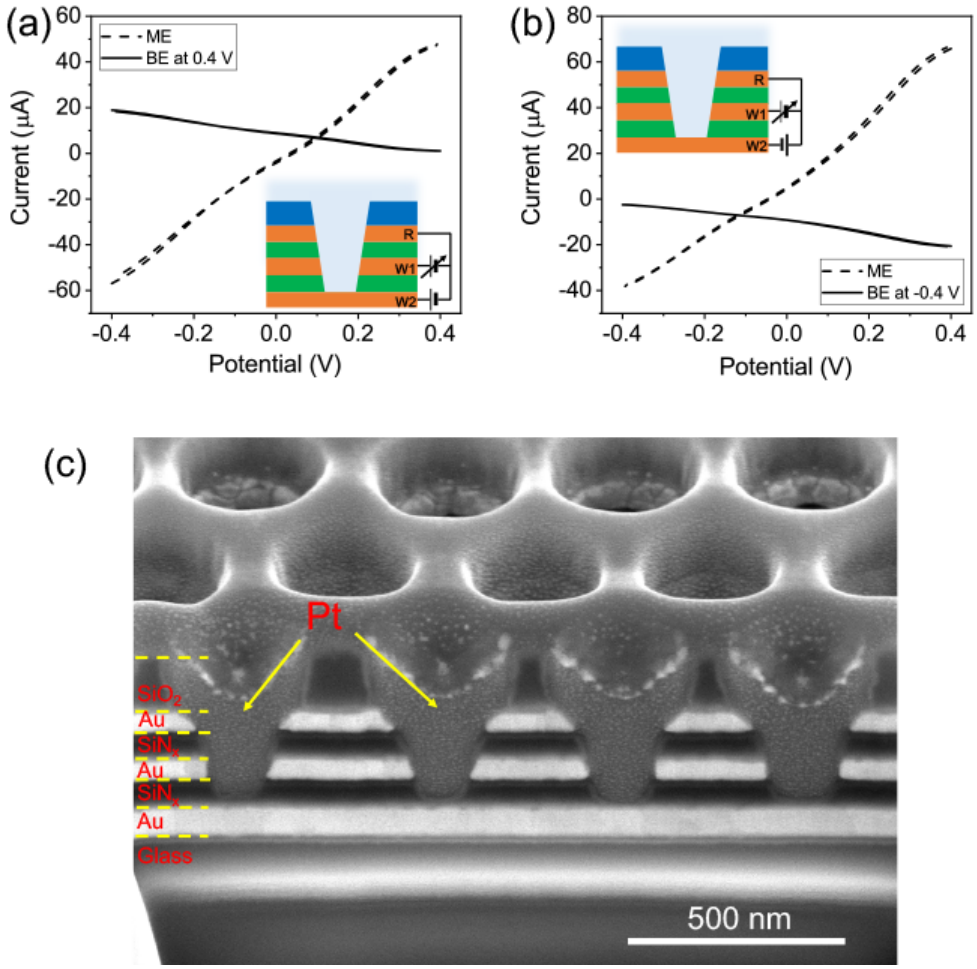

Figure S11. (a,b) Voltammograms of 100 mM $Fe(CN)_6^{3/4-}$ in 1 M KNO_3 at E_{BE} = +0.4 V (a) and –0.4 V (b) while sweeping ME between ±0.4 V against TE reference. (c) A cross-sectional SEM image showing the nanopore structure, in which all three electrodes (ring, ring, and disk) are directly exposed to the nanopore space.

References

[1] K. Fu, D. Han, S.-R. Kwon, P. W. Bohn, *ACS Nano* **2018**, *12*, 9177.

[2] S.-R. Kwon, K. Fu, D. Han, P. W. Bohn, *ACS Nano* **2018**, *12*, 12923.